



## 10    **Abstract**

11    **Temporal experience of odor gradients is important in spatial orientation of animals. The fruit fly**  
12    ***Drosophila melanogaster* exhibits robust odor-guided behaviors in an odor gradient field. In order**  
13    **to investigate how early olfactory circuits process temporal variation of olfactory stimuli, we**  
14    **subjected flies to precisely defined odor concentration waveforms and examined spike patterns of**  
15    **olfactory sensory neurons (OSNs) and projection neurons (PNs). We found a significant temporal**  
16    **transformation between OSN and PN spike patterns, manifested by the PN output strongly**  
17    **signaling the OSN spike rate and its rate of change. A simple two-dimensional model admitting the**  
18    **OSN spike rate and its rate of change as inputs closely predicted the PN output. When cascaded**  
19    **with the rate-of-change encoding by OSNs, PNs primarily signal the acceleration and the rate-of-**  
20    **change of dynamic odor stimuli to higher brain centers, thereby enabling animals to reliably**  
21    **respond to the onsets of odor concentrations.**

22

## 23    **Introduction**

24    Odor distribution in nature is intermittent and dynamic (Murlis et al., 1992; Vickers et al., 2001), and  
25    animals have evolved the ability to detect and respond to temporal variation of odor stimuli (Vickers et  
26    al., 2001; David et al., 1983; Thesen et al., 1993; Porter et al., 2007; Semmelhack and Wang 2009; Kato  
27    et al., 2014). In one of the most sophisticated examples, *Drosophila* larvae with only a single functional  
28    OSN are capable of moving toward a droplet of an attractive odor by actively orienting themselves  
29    (Louis et al., 2008). Similarly, adult fruit flies exhibit robust odor-guided behaviors such as turning  
30    upwind in flight upon contact with an attractive odor plume (Budick and Dickinson, 2006) and staying  
31    within a specific odor zone (Semmelhack and Wang, 2009). In order to enable such odor-guided tasks, it

is essential for any olfactory system to process time-varying features of olfactory stimuli and supply behaviorally-relevant information to higher brain centers.

Several recent studies have investigated how dynamic olfactory stimuli are processed in insect early olfactory systems (systems consisting principally of OSNs and PNs) and observed significant temporal processing of odor signals (Kim et al., 2011; Nagel and Wilson, 2011; Geffen et al., 2009; Bhandawat et al., 2007; Martelli et al., 2013). Most of these studies employed a simple odor delivery system that generated step-pulse-like odor stimuli without directly monitoring the actual odor concentration levels. For a rigorous understanding of sensory processing, however, it is essential to precisely measure the input stimuli and systematically explore the input space, as has been successfully done in the field of vision and audition (Wu et al., 2006). Moreover, natural odor plumes are encountered in various spatio-temporal patterns, and their dynamics and statistics can influence the neural encoding mechanism (Vickers et al., 2001; Brenner et al., 2000).

In *Drosophila*, OSNs expressing the same receptors connect with PNs in one of roughly 50 spherical compartments, termed olfactory glomeruli, which constitute a deutocerebral neuropil called the antennal lobe. PNs subsequently relay olfactory information to higher brain centers such as the mushroom body and the lateral horn (Stocker et al., 1990).

Two recent studies independently reported that *Drosophila* OSNs encode not only the odor concentration but also its rate of change as a function of time (Kim et al., 2011; Nagel and Wilson, 2011). Building on this recent advance, we asked how PNs further contribute to creating internal representations of dynamic olfactory environments. We tested OSNs and PNs with short plume-like

55 odor stimuli in a variety of settings and analyzed the correlation structure of input/output signals in the  
56 odor-OSN-PN pathway. We also constructed a two-dimensional (2D) linear-nonlinear (LN) model of  
57 the OSN-to-PN transformation by inducing an ensemble of triangle-shaped OSN spike rates via a  
58 systematic design of olfactory stimuli.

59

60

## 61 **Results**

62 We employed a novel odor delivery system that can reliably produce various odor concentration  
63 waveforms and provide measurements of the odor concentration with a millisecond resolution on every  
64 experiment trial (Figure 1A,B) (Kim et al., 2011). Various odor concentration profiles were designed  
65 and tested (Figure 1 – figure supplement 1), and the corresponding OSN and PN responses were  
66 measured in two separate assays sharing the same odor delivery system (Figure 1A,B). The observed  
67 odor concentrations were closely matched between the two assays (Figure 2A-C). We used acetone as  
68 the primary odorant because its low ionization potential afforded a high signal-to-noise ratio in our odor  
69 concentration measurements. We tested a pair of directly-connected OSNs and PNs innervating the  
70 DM4 glomerulus with five different acetone concentration waveforms. The dynamics of OSN and PN  
71 responses differed significantly from their respective feedforward inputs, and all responses initiated  
72 within a few tens of milliseconds of the odor onset (Figure 1C). PNs generally showed a bigger peak  
73 spike rate and exhibited more phasic spiking patterns than the presynaptic OSNs. However, the exact  
74 functional transformation between OSNs and PNs could not be readily assessed due to the complex  
75 dynamics of OSN and PN signals.

76

77 We therefore designed a set of elementary odor concentration waveforms: a step, a ramp and a parabola  
78 (top row of Figure 2A-C). We reasoned that the simple nature of these waveforms would facilitate the  
79 analysis of the input/output relationship.

80

81 Consistent with previous reports (Kim et al., 2011; Nagel and Wilson, 2011), OSNs responded most  
82 strongly to polynomial waveforms when the odor concentration rose rapidly. For the ramp and parabola  
83 odor signals, OSN responses were the exact rate-of-change function of their input: a step output to a  
84 ramp input (Figure 2B,E) and a ramp output to a parabola input (Figure 2C,F). This pattern of encoding  
85 was preserved for different combinations of odorants and OSN-PN pairs (Figure 2 – figure supplement  
86 1). To look into this observation formally, we measured the similarity between three different input  
87 features – concentration amplitude, rate-of-change, and acceleration – and the output spike rate of OSNs  
88 by performing a set of cross-correlation analyses. The correlation was strong between the OSN output  
89 and both odor concentration and its rate of change, but weak between the OSN output and the  
90 acceleration of odor concentration (Figure 2J).

91

92 Given the very same panel of olfactory stimuli, PN responses exhibited bigger peak amplitude and more  
93 stereotyped temporal patterns than OSNs (Figure 2G-I). All PN responses transiently peaked at the time  
94 of the odor onset, and their peak times were advanced from the OSN peak times (See also Figure 4).  
95 Specifically, in response to ramp-shaped OSN signals, PNs exhibited a rapid step response (Figure 2F,I).  
96 To step-like OSN signals, PN showed a phasic onset response, followed by a tonic spiking pattern  
97 (Figure 2E,H). These input/output relationships are reminiscent of the rate-of-change encoding in the  
98 odor-to-OSN transformation, where the ramp and step odor signals were similarly transformed.  
99 Biophysically, this phenomenon suggests a rapid adaptation between OSNs and PNs, which is in

100 agreement with previous reports demonstrating strong short-term depression in synapses between OSNs  
101 and PNs (Kazama and Wilson, 2008; Kazama and Wilson, 2009; Nagel et al., 2015). From a modeling  
102 perspective, this observation predicted a strong correlation between the PN spike rate and the rate-of-  
103 change of the OSN spike rate. A correlation analysis between the PN output and three different input  
104 features – OSN spike rate, rate-of-change, and acceleration – confirmed this prediction (Figure 2K).  
105 Together, this supports the hypothesis that PN responses can be modeled as a function of the OSN spike  
106 rate and its rate of change, at least for the tested class of odor stimuli.

107

108 We therefore propose a simple model of the OSN-to-PN transformation comprising two input blocks:  
109 the OSN spike rate and its rate of change, followed by a two-dimensional (2D) nonlinearity that maps  
110 these inputs into the PN spike rate (Figure 3D). The model has the structure of a classical 2D linear-  
111 nonlinear model with its linear blocks postulated as amplitude and rate-of-change filters (Brenner et al.,  
112 2000; Geffen et al., 2009). Given the hypothesized input blocks, the model can be fully identified by  
113 estimating the nonlinear block from experimental data. The validity of the model can be tested by  
114 assessing its ability to predict the PN response to new odor waveforms. In order to estimate the  
115 nonlinearity, we first designed OSN spike activity profiles that explore the hypothesized PN input space  
116 with an efficient sampling grid. An ensemble of triangle-shaped inputs was shown to be suitable for this  
117 purpose, since each up/down ramp stimulus tests the target system with a distinct pair of positive and  
118 negative gradients while also sweeping a wide range of input amplitudes (Kim et al., 2011).

119

120 How can we induce an ensemble of triangle signals at the OSN output? We fine-tuned odor  
121 concentration signals, while observing the OSN spike rate, until the desired OSN spike rates were  
122 produced (Figure 3A). The odor concentration signals inferred from this method are an ensemble of

123 parabolas with systematically varying peak times and amplitudes (Figure 3A). The 2D nonlinearity was  
124 estimated subsequently by running a ridge regression analysis on spike rate samples from the OSN and  
125 PN signals (Kim et al., 2011) (Figure 3BC).  
126  
127 The estimated 2D nonlinearity showed a strong dependency on the rate-of-change of OSN spike rate  
128 (Figure 3BC). When the nonlinearity was estimated for samples with a fixed odor concentration value,  
129 the PN spike rate rose almost linearly with respect to the rate-of-change (Figure 3 – figure supplement  
130 1). However, the gain of the PN output with respect to the OSN rate-of-change decreased monotonically  
131 with concentration, suggesting that at least a 2D model is required to describe the OSN-to-PN  
132 transformation (Figure 3 – figure supplement 1). We tested the model by comparing the simulated  
133 model output with the experimental PN spike activity (Figure 3C). With step, ramp, and parabola odor  
134 inputs, the experimental outputs were closely matched by the model (root mean square error = 25  
135 spike/s, Figure 3F). While the odor-evoked responses were well matched by the model, including peak  
136 times and amplitudes, the model output often overestimated the actual PN spike rate before and after the  
137 stimulus interval. This is because the estimated nonlinearity exhibits a relatively high slope at low input  
138 amplitudes (Figure 3 – figure supplement 1), which renders the system highly sensitive to the noisy  
139 fluctuations at low OSN spike rates (Pahlberg and Sampath, 2011). This problem is thought to be  
140 mitigated in olfactory glomeruli by pooling input from a population of OSNs, thereby achieving a higher  
141 signal-to-noise ratio than provided by a single OSN (Bhandawat et al., 2007). In summary, the proposed  
142 simple 2D model provides a decent approximation of the OSN-to-PN transformation and corroborates  
143 the notion that PNs mainly encode OSN spike rate and its rate of change in a nonlinear fashion.  
144

145 What is the functional consequence of acceleration encoding by antennal lobe PNs? In signal processing  
146 theory, the time derivative, or rate-of-change operation, advances the phase of a time signal. For  
147 example,  $\cos(t)$  is the time derivative of  $\sin(t)$ , and its phase is advanced by  $\pi/2$ . Similarly, the rate-of-  
148 change of a sample triangle-shaped signal shows an advancement of a peak time, and its acceleration  
149 exhibits a peak time that is further advanced (Figure 4A). Therefore, we reasoned that the computation  
150 of the first and second time derivative (rate-of-change and acceleration) of odor concentrations by OSN  
151 and PNs, respectively, act to advance peak times of olfactory stimuli. To investigate this idea with a  
152 larger set of odor stimuli, we designed a set of triangle-shaped odor waveforms with peak times varying  
153 uniformly between 0.6 s and 1.7 s after the stimulus onset (Figure 4B, ‘odor’ curve in Figure 4C). As  
154 shown in the previous experiments with triangle-shaped stimuli (Figure 2B), OSNs responded in a  
155 pulse-shaped pattern (Figure 4B), with the peak response advanced by 400–1000 ms relative to the  
156 stimulus peak (‘OSN’ curve in Figure 4C). In response to the same panel of odor stimuli, PNs  
157 consistently produced peak output (Figure 4B) at around 200 ms after the stimulus onset, regardless of  
158 the dynamics of the odor/OSN signals (‘PN’ curve in Figure 4C). For the parabola-shaped odor stimuli  
159 (Figure 3A), the peak OSN and PN responses were similarly advanced in time relative to the odor and  
160 OSN peaks (right plot in Figure 4C) but were more variable. The advancement of a peak time was  
161 previously reported for step-pulse odor stimuli (Bhandawat et al., 2007), and our work confirms this  
162 result for a larger set of dynamically varying odor stimuli. Together, we hypothesize that acceleration  
163 encoding in the *Drosophila* antennal lobe allows higher olfactory centers to rapidly respond to onsets of  
164 slowly rising odor stimuli.

165  
166  
167



## 168 **Discussion**

169 We tested first- and second-order neurons in the *Drosophila* olfactory system with a wide range of  
170 dynamically-varying odor concentrations and constructed a simple 2D linear-nonlinear model for the  
171 temporal processing of olfactory information. The shape of the 2D nonlinearity and the relatively low  
172 prediction error of the model support the hypothesis that the PN spike rate is most strongly dependent on  
173 the rate-of-change of its feedforward OSN input. When combined with the dynamic sensory encoding  
174 by OSNs – encoding of odor concentration and its rate of change – PNs signal the rate-of-change and,  
175 most strongly, the acceleration of odor concentration signals to higher brain centers. One remarkable  
176 example of the ‘acceleration encoding’ by PNs is found in the OSN/PN responses to the parabolically  
177 rising odor input, where the onset is enormously amplified to create step-like responses in PNs (Figure  
178 2C,I).

180 To the best of our knowledge, the encoding of acceleration by an olfactory sensory system has not been  
181 demonstrated elsewhere. This sensory encoding mechanism is distinguished from other chemosensory  
182 systems. For example, in bacterial chemotaxis, the rate-of-change of a stimulus is computed and fed  
183 directly into its motor system that controls the flagellar rotation (Bourret et al., 1991). The nematode *C.*  
184 *elegans* also exhibits a local-gradient-based chemotaxis behavior, and neurons in its sensorimotor  
185 pathway are shown to compute the rate-of-change of concentration gradients (Suzuki et al., 2008).

187 Why do fruit flies compute acceleration of odor concentrations? How is the acceleration of an olfactory  
188 stimulus relevant to a fly’s chemotaxis? An efficient chemotaxis strategy should depend on the  
189 distribution of odor molecules in the behaviorally relevant range, which can be quantified using a  
190 Reynolds number (Weissburg, 2000). Habitats of both nematodes and bacteria have low Reynolds  
191 numbers ( $Re < 1$ ), and thus the odor distribution is primarily determined by a diffusion process. In this

environment, the steepest local odor gradient can be directly linked to the location of the odor source, and therefore animals in such environments are expected to encode the rate-of-change of odor concentrations in order to detect the steepest gradient. In contrast, flying insects experience fluid mechanics that have relatively high Reynolds numbers ( $Re > 10$ ), with turbulence dictating the distribution of odor molecules over the diffusion process. In this regime, the local odor gradient within an odor plume would be less informative in determining the location of the odor source, than the distribution of odor plumes over a macroscopic scale. In fact, it has been well established that insects, including fruit flies, use a strategy of turning upwind during odor plume encounters, a strategy that does not require interpreting local concentration gradients (Budick and Dickinson, 2006).

Furthermore, the relative position of a flying animal and the distribution of odor plumes evolve rapidly over time. It is therefore crucial for flying insects to detect and respond to an encountered odor plume before the fly's position drifts relative to adjacent plumes. We showed that *Drosophila* early olfactory system signals the acceleration of odor concentrations to higher brain centers. This encoding mechanism allows an animal to detect the odor onset at a very early phase (Figure 4). Therefore, it is tempting to speculate that the acceleration encoding has evolved in *Drosophila* to maximize its chance to locate the odor source in a turbulent environment.

It has also been shown that fruit flies can respond to the spatial difference of the odor concentration between two antennae in both walking and flight (Duistermars et al., 2009; Gaudry et al., 2013).

However, even with the lack of the spatial sampling ability, fruit fly larvae can locate an odor source, based on the temporal sampling of odor gradients (Louis et al., 2008). Therefore, adult fruit flies may rely on both spatial and temporal sampling methods to locate an odor source, although their relative

215 importance may vary depending on the locomotive state as Reynolds numbers are different between  
216 walking and flight.

217

218

## 219 **Materials and methods**

### 220 **Odor delivery**

221 We built a precise and versatile odor delivery system (Kim et al., 2011). An odorant was diluted in  
222 dipropylene glycol, and 20 mL of the resulting mixture was put into a glass vial (30 mL) and  
223 subsequently sealed by a screw cap with a silicone septa. Inlet and outlet needles were inserted into the  
224 vial headspace. The saturated vapor in this headspace was puffed by directing a low-flow air stream  
225 ( $\leq 100$  mL/min) from an air cylinder (UN1002, TechAir) into the odor vial by opening inlet and outlet  
226 solenoid valves (Series 10, Parker-Hannifin Corporation). Subsequently, the outlet needle carried the  
227 saturated vapor from inside the vial to a custom laminar mixer where the odor flow was combined with a  
228 strong carrier flow (800 mL/min). The mixer was carefully designed so as to minimize the turbulence  
229 that could be formed when the low-flow odor stream is added to a high-flow-rate carrier stream. The  
230 output of the mixer was then directed to the antennae and maxillary palps of a prepared animal through a  
231 glass capillary (1mm inner diameter). The interval between two consecutive puffs was between 45 s and  
232 70 s depending on the amount of vapor consumed in each puff, and the mixture was replenished about  
233 every 10 trials. All flows were electronically controlled by a miniature pressure controller (VSO-EP,  
234 Parker-Hannifin, OH) and measured using a digital flow meter (PV9000, Key Instruments, PA) in real  
235 time. After hitting the animal, the odor flow was immediately sucked into a probe and measured by a  
236 photo-ionization detector (PID, Aurora Scientific, Canada) with 1L/min flow rate. The output of the PID  
237 was digitally sampled at 10 kHz and later advanced by 2 ms in order to compensate for the latency

caused by the suction probe. In order to convert the PID output voltage into the odor concentration in parts per million (ppm), we regularly (every 10 trials) measured the output of the PID with a calibration odor (3% propylene) and estimated the general sensitivity of the PID, which gradually decays over time. The PID sensitivity ratio of actual odor to standard odor was measured in a separate experiment with a fully saturated odor vapor and used to calculate a scaling factor between the PID output (in Volts) and the absolute odor concentration (in ppm) (Kim et al., 2011).

### ***Drosophila* stocks**

*Drosophila* stocks were maintained at a room temperature on a 12-hour light/12-hour dark schedule and kept in standard plastic vials containing a cornmeal-agar medium. All experiments were carried out with female flies of the *NP3062-GAL4/NP3062-GAL4;UAS-mCD8::GFP/UAS-mCD8::GFP;+/+* genotype. *NP3062-GAL* flies were kindly provided by Kei Ito.

### **Electrophysiology**

Female flies 2-5 days post-eclosion were used for both OSN and PN recordings. For the OSN recordings, single basiconic sensilla were targeted with electrolytically-sharpened tungsten electrodes to measure the aggregate electrical activity of OSNs housed in these sensilla (Figure 1B) (Kim et al., 2011). Recordings were analyzed by a custom MATLAB code (Source code 1) to sort out action potentials from Or59b or Or7a OSNs (Kim et al., 2011). For the PN recordings, a female fly was gently immobilized beneath a cellulose acetate film with an adhesive (Datta et al., 2008). The film was then carefully transferred to a petri dish in which a circular hole was made at the center. When placing an animal in the hole, the location of the head was carefully adjusted so that the antennae and maxillary palps were located strictly within the odor stream between the odor delivery tubing and the suction probe,

261 both of which were embedded in the petri dish. Antennal lobes were exposed by gently removing a head  
262 cuticle as well as the film under saline solution containing 108 mM NaCl, 5 mM KCl, 2 mM CaCl<sub>2</sub>, 8.2  
263 mM MgCl<sub>2</sub>, 4 mM NaHCO<sub>3</sub>, 1 mM NaH<sub>2</sub>PO<sub>4</sub>, 5 mM trehalose, 10 mM sucrose, and 5 mM HEPES (pH  
264 7.5, 265 mOsm) (Wang et al., 2003). In order to access the PN somas, the perineural sheath was  
265 weakened by a 1-2 min treatment with 1mg/mL collagenase (Type I Collagenase, Sigma-Aldrich). The  
266 dorsal part of the sheath was then gently ruptured by a sharp quartz glass electrode using a micro-  
267 manipulator (MP-285, Sutter Instrument, CA). A ground electrode was placed into the saline solution  
268 and connected to a headstage amplifier (CV-7B, Molecular Devices, CA).

269  
270 In order to record action potentials of a single PN, a borosilicate patch electrode (7–10 MΩ tip  
271 resistance) filled with saline solution was attached to the target cell and gentle suction was applied  
272 through the electrode capillary until a loose seal (50–100 MΩ) was formed. The current was amplified  
273 (MultiClamp 700B, Molecular Devices, CA), low-pass filtered at 1.2 kHz, sampled at 10 kHz (Digidata  
274 1322A, Axon Instruments), and stored on a computer by software (Clampex, Molecular Devices, CA).  
275 The animal was alive and active for a few hours as indicated by the spontaneous extension of its legs.  
276 Fresh oxygenated saline solution was perfused throughout the experiment. Finally, the PNs innervating  
277 the DM4 and DL5 glomeruli were identified by genetic means, using an enhancer-trap line expressing  
278 GFP in these cells. The identity of recorded cells was further verified by their odor response and the  
279 location of the soma in the dorsal cluster of the antennal lobe. Spike sequences were detected and sorted  
280 offline using custom software (Source code 1), written in MATLAB (Mathworks, MA).

281  
282 **Estimating spike rates, rate-of-change and acceleration signals**

283 Spike rates of OSNs and PNs were estimated by constructing a peri-stimulus time histogram (PSTH)  
 284 with a 100 ms bin size and a 75 ms overlap between adjacent bins. For the correlation analysis and 2D  
 285 model prediction, the rate-of-change and acceleration components of odor and OSN traces were  
 286 estimated by a forward difference equation, with the difference time interval as the scaling factor; i.e.,  
 287  $\frac{dx}{dt}=[x(t-\Delta)-x(t)]/\Delta$ , where  $x$  represents either the odor concentration or the OSN response, and  $\Delta$   
 288 denotes the time interval. The time interval was 50 ms for the odor rate-of-change, 100 ms for the odor  
 289 acceleration, the OSN rate-of-change and the OSN acceleration. Since the output of the forward  
 290 difference equation is sensitive to high-frequency components of the signal, we low-pass filtered the  
 291 amplitude and rate-of-change signals before deriving the rate-of-change and acceleration, respectively.  
 292 Cut-off frequencies of the low-pass filters were 20 Hz for the odor amplitude, 10 Hz for the odor rate-of-  
 293 change, 4 Hz for the OSN spike rate, and 4 Hz for the OSN rate-of-change.

## 294

### 295 **Cross-correlation analyses between input features and OSN/PN output**

296 The cross-correlation coefficient,  $\rho(x,y)$  between an input  $x$  and the corresponding output  $y$  was  
 297 computed as a normalized cross-covariance function; that is,

$$298 \quad \rho(x,y) = \frac{\frac{1}{N} \sum_{i=1}^N (x[i] - \mu_x)(y[i] - \mu_y)}{\sigma_x \sigma_y},$$

299 where  $\mu$  and  $\sigma$  are respectively the mean and standard deviation of the variable in the subscript.

300

### 301 **Estimating the 2D nonlinearity**

302 We hypothesized a nonlinear function  $f(\cdot, \cdot)$  that takes inputs from the OSN spike rate  $y$  and its rate-of-  
 303 change  $dy/dt$  and whose output corresponds to the PN spike rate  $z$ ; i.e.,

$$z=f(y, \frac{dy}{dt}),$$

and  $f(.,.)$  was estimated using a 2D ridge regression method on 100×100 grids (Kim et al., 2011).

## Acknowledgements

The work presented here was supported by NIH under grant number R01DC008701-05 and was conducted in the Axel laboratory at Columbia University. The authors would like to thank Dr. Richard Axel for his outstanding support.

## Author contributions

A.J.K., A.A.L. and Y.B.S designed the experiments and wrote the manuscript. A.J.K. and Y.B.S. performed experiments and spike train analysis. A.J.K. designed and performed analyses in the manuscript.

## References

**Bhandawat V**, Olsen SR, Gouwens NW, Schlieff ML, Wilson RI. 2007. Sensory processing in the *Drosophila* antennal lobe increases reliability and separability of ensemble odor representations. *Nature Neuroscience* **10**:1474–1482. doi: 10.1038/nn1976.

324 **Bourret RB**, Borkovich KA, Simon MI. 1991. Signal transduction pathways involving protein  
 325 phosphorylation in prokaryotes. *Annual review of biochemistry* **60**:401-441. doi:  
 326 10.1146/annurev.bi.60.070191.002153

327 **Brenner N**, Bialek W, de Ruyter van Steveninck R. 2000. Adaptive rescaling maximizes information  
 328 transmission. *Neuron* **26**:695–702. doi: 10.1016/S0896-6273(00)81205-2.

329 **Budick SA**, Dickinson MH. 2006. Free-flight responses of *Drosophila melanogaster* to attractive odors.  
 330 *Journal of Experimental Biology* **209**:3001–3017. doi: 10.1242/jeb.02305.

331 **Datta SR**, Vasconcelos ML, Ruta V, Luo S, Wong A, Demir E, Flores J, Balonze K, Dickson BJ, Axel  
 332 R. 2008 The *Drosophila* pheromone cVA activates a sexually dimorphic neural circuit. *Nature* **452**:473–  
 333 477. doi: 10.1038/nature06808:

334 **David CT**, Kennedy JS, Ludlow AR. 1983. Finding of a sex pheromone source by gypsy moths released  
 335 in the field. *Nature* **303**:804–806. doi: 10.1038/303804a0.

336 **Duistermars BJ**, Chow DM, Frye MA. 2009. Flies require bilateral sensory input to track odor  
 337 gradients in flight. *Current Biology*, **19**:1301-1307. doi: 10.1016/j.cub.2009.06.022

338 **Gaudry Q**, Hong EJ, Kain J, de Bivort BL, Wilson RI. (2013). Asymmetric neurotransmitter release  
 339 enables rapid odour lateralization in *Drosophila*. *Nature*, **493**:424–428. doi: 10.1038/nature11747

340 **Geffen MN**, Broome BM, Laurent G, Meister M. 2009. Neural encoding of rapidly fluctuating odors.  
 341 *Neuron* **61**:570–586. doi: 10.1016/j.neuron.2009.01.021.

342 **Kato S**, Xu Y, Cho CE, Abbott LF, Bargmann CI. 2014. Temporal responses of *C. elegans*  
 343 chemosensory neurons are preserved in behavioral dynamics. *Neuron* **65**:171–178. doi:  
 344 10.1016/j.neuron.2013.11.020.

345 **Kazama H**, Wilson RI. 2008. Homeostatic matching and nonlinear amplification at identified central  
 346 synapses. *Neuron* **58**:401-413. doi: 10.1016/j.neuron.2008.02.030.



347 **Kazama H**, Wilson RI. 2009. Origins of correlated activity in an olfactory circuit. *Nature Neuroscience*  
348 **12**:1136-1144. doi: 10.1038/nn.2376.

349 **Kim AJ**, Lazar AA, Slutskiy YB. 2011. System identification of *Drosophila* olfactory sensory neurons.  
350 *Journal of Computational Neuroscience*, **30**:143–161. doi: 10.1007/s10827-010-0265-0.

351 **Louis M**, Huber T, Benton R, Sakmar TP, Vosshall LB. 2008. Bilateral olfactory sensory input  
352 enhances chemotaxis behavior. *Nature Neuroscience* **11**:187–199. doi: 10.1038/nn2031.

353 **Martelli C**, Carlson JR, Emonet T. 2013. Intensity invariant dynamics and odor-specific latencies in  
354 olfactory receptor neuron response. *Journal of Neuroscience* **33**:6285-6297, doi:  
355 10.1523/JNEUROSCI.0426-12.2013.

356 **Murlis J**, Elkinton JS, Carde RT. 1992. Odor plumes and how insects use them. *Annual review of*  
357 *entomology* **37**: 505–532. doi: 10.1146/annurev.en.37.010192.002445.

358 **Nagel KI**, Wilson RI. 2011. Biophysical mechanisms underlying olfactory receptor neuron dynamics.  
359 *Nature neuroscience* **14**:208–216. doi: 10.1038/nn.2725.

360 **Nagel KI**, Hong EJ, Wilson RI. 2015. Synaptic and circuit mechanisms promoting broadband  
361 transmission of olfactory stimulus dynamics. *Nature Neuroscience* **18**:56–65. doi: 10.1038/nn.3895.

362 **Pahlberg J**, Sampath AP (2011). Visual threshold is set by linear and nonlinear mechanisms in the  
363 retina that mitigate noise. *Bioessays*, **33**:438-447. doi: 10.1002/bies.201100014.

364 **Porter J**, Craven B, Khan RM, Chang SJ, Kang I, Judkewitz B, Judkewicz B, Volpe J, Settles G, Sobel  
365 N. 2007. Mechanisms of scent-tracking in humans. *Nature Neuroscience* **10**: 27–29. doi:  
366 10.1038/nn1819.

367 **Semmelhack JL**, Wang JW. 2009. Select *Drosophila* glomeruli mediate innate olfactory attraction and  
368 aversion. *Nature* **459**:218–223. doi: 10.1038/nature07983.

369 **Stocker RF**, Lienhard MC, Borst A, Fischbach KF. 1990. Neuronal architecture of the antennal lobe in  
370 *Drosophila melanogaster*. *Cell and Tissue Research* **262**:9–34. doi: 10.1007/BF00327741.

371 **Suzuki H**, Thiele TR, Faumont S, Ezcurra M, Lockery SR, Schafer WR. 2008. Functional asymmetry  
372 in *Caenorhabditis elegans* taste neurons and its computational role in chemotaxis. *Nature* **454**:114-117.  
373 doi: 10.1038/nature06927

374 **Thesen A**, Steen JB, Doving KB. 1993. Behaviour of dogs during olfactory tracking. *Journal of*  
375 *Experimental Biology* **180**:247-251.

376 **Vickers N**, Christensen T, Baker T, Hildebrand J. 2001. Odour-plume dynamics influence the brain's  
377 olfactory code. *Nature* **410**:466–470. doi: 10.1038/35068559.

378 **Wang J**, Wong A, Flores J, Vosshall L, Axel R. 2003. Two-photon calcium imaging reveals an odor-  
379 evoked map of activity in the fly brain. *Cell* **112**: 271–282. doi: 10.1016/S0092-8674(03)00004-7.

380 **Weissburg MJ**. 2000. The fluid dynamical context of chemosensory behavior. *The Biological Bulletin*  
381 **198**:188-202.

382 **Wu M**, David S, Gallant J. 2006. Complete functional characterization of sensory neurons by system  
383 identification. *Annual Review of Neuroscience* **29**:477–505. doi:  
384 10.1146/annurev.neuro.29.051605.113024.

## 385 **Figure Legends**

386 **Figure 1.** Dynamics of sample odor stimuli are significantly transformed along an odor-OSN-PN  
387 pathway. (A) An experimental setup. Activity of OSNs and PNs was recorded in two different assays,  
388 which share the same odor delivery system. A photoionization detector (PID) provided real-time  
389 measurements of odor concentrations in every trial. (B) Sample traces of OSN and PN responses to a  
390 triangle-shaped odor concentration profile. (C) Sample OSN and PN responses to five distinct odor  
391 concentration waveforms. (top row) Odor concentration profiles. Each trace is an average of six  
392 interleaved trials, recorded in the OSN assay. (middle row) Raster and peri-stimulus time histogram  
393 (PSTH) plots of the Or59b OSN response. (bottom row) Raster and PSTH plots of the postsynaptic  
394 DM4 PN response to the same panel of odor stimuli.

395 **Figure 2.** Correlation structures of olfactory information representations in odor, OSN and PN signals.  
396 (A-C) Three polynomial odor stimuli: a pulse, a ramp and a parabola. Light gray lines represent  
397 individual trials from five different OSN experiments, and dark gray lines represent individual traces  
398 from five different PN experiments. Blue and red lines are average traces respectively from the OSN and  
399 PN experiments. An 'L' mark in magenta at the bottom left corner of each panel represents the zero  
400 amplitude point. (D-F) Or59b OSN response to the above stimuli (n=5 flies). (G-I) PN response to the  
401 same set of stimuli (n=5 flies). (J-L) Correlation analyses between three pairs of input and output (amp:  
402 amplitude, roc: rate-of-change, acc: acceleration). OSNs and PNs mainly encode the amplitude and rate-  
403 of-change of their feedforward inputs, whereas PNs most strongly represent the acceleration and rate-of-  
404 change components of the odor input. Results with error bars indicate mean  $\pm$  standard deviation, and  
405 \*\*\* indicates  $P < 0.001$  (t-test). n=9 flies for each analysis, 5 flies from the above traces and 4 flies from  
406 the same experiment at half concentration (data not shown).

**Figure 3.** A simple 2D model characterizes the OSN-to-PN transformation. **(A)** Input/output traces used in modeling the OSN-to-PN transformation (n=5 trials for both OSN and PN data). An ensemble of triangle-shaped OSN spike rates (middle) were designed as a direct *in vivo* input to the PNs. These OSN spiking patterns were induced by an ensemble of parabola odor inputs (top). **(B)** Input and output samples for the 2D nonlinearity block. Input axes are OSN spike rate and its rate-of-change, and the output is the PN spike rate. The samples were estimated from the OSN and PN spike trains with 25 ms sampling interval and depicted as a red dot in the input/output space. **(C)** A 2D nonlinearity was estimated by ridge regression method from the samples marked in **(B)**. **(D)** A simple 2D model of the OSN-to-PN transformation, as a 2D linear-nonlinear model. **(E)** The 2D model was tested for a set of OSN spike rates to evaluate its predictive ability. The black surface depicts a three-dimensional rendering of the 2D nonlinearity in **(B)**. Six OSN spike rates — five triangle-shaped signals and one step pulse-shaped input — and their rate-of-change functions were projected to the surface. Amplitude readouts from the trajectories on the surface constitute the simulated PN output. The step pulse-shaped input was introduced for cross-validation of the model since this input was not used for building the model. **(F)** The predicted PN spike rate closely followed the magnitude and dynamics of the experimental PN spike rate, for six OSN spike rate inputs (insets). The average prediction errors are 31, 26, 21, 21, 23, 29 spike/s (clockwise from the top left corner, in root-mean-square-error).

**Figure 4.** A cascade of rate-of-change encodings leads to a rapid detection of the stimulus onset. **(A)** A cascade of two rate-of-change transformations leads to the advancement of the peak time near to the

stimulus onset, in response to a triangle-shaped input. At each stage, the rate-of-change of the input was computed, and the output was half-wave rectified. **(B)** 8 triangle-shaped acetone concentration waveforms (left) and the corresponding OSN and PN responses. **(C)** The peak times for odor, OSN, and PN signals. The advancement in peak times was observed in both the odor-to-OSN and OSN-to-PN transformations. Peak times were color-coded so that the color of the marker matches that of the associated triangle signals in **(B)** and parabola signals in Figure 3(A). n=5 OSNs and n=4 PNs for both triangles and parabolas. Results with error bars indicate mean  $\pm$  standard deviation.

**Figure 1 – Figure supplement 1.** Sample traces of 17 acetone odor concentration waveforms and their responses in Or59b OSNs and DM4 PNs. Each trace represents an average of 4-6 trials, and the odor concentration was measured in the OSN assay. An ‘L’ mark in magenta at the bottom left corner of each panel represents the zero amplitude point and zero time point for each stimulus epoch.

**Figure 2 – Figure supplement 1.** The patterns of the dynamic odor encoding were preserved for different combinations of odorants and OSN-PN pairs. **(A)** Outputs of an Or59b OSN and a DM4 PN in response to methyl butyrate polynomial odor inputs. Gray areas represent the standard deviation of the estimated OSN/PN output. **(B)** Outputs of an Or7a OSN and a DL5 PN in response to butanal polynomial odor inputs. Gray areas represent the standard deviation of the estimated OSN/PN output.

446

447 **Figure 3 – Figure supplement 1.** PN output is dependent on both OSN spike rate and its rate of change.

448 (A) The triangle-shaped OSN spike rate (top), its rate of change (middle), and the corresponding PN  
449 spike rates (bottom). At a fixed OSN spike rate (60 spike/s, a solid red line in the top panel), the PN  
450 spike rate varies from 0 to 280 spike/s depending on the rate-of-change value of the OSN spike rate. (B)  
451 At a fixed OSN spike rate (blue line for 30 spike/s, red line for 60 spike/s, green line for 120 spike/s, as  
452 depicted in (A)), the PN spike rate is linearly related to the rate-of-change value of the OSN spike rate  
453 with half-wave rectification in the negative rate-of-change interval. (C) The gain  $\beta$  of the PN response,  
454 with respect to the rate-of-change of the OSN output, decreases with increasing input amplitude.

455

456 **Source code 1.** Custom software written in MATLAB for the analysis of OSN and PN data.

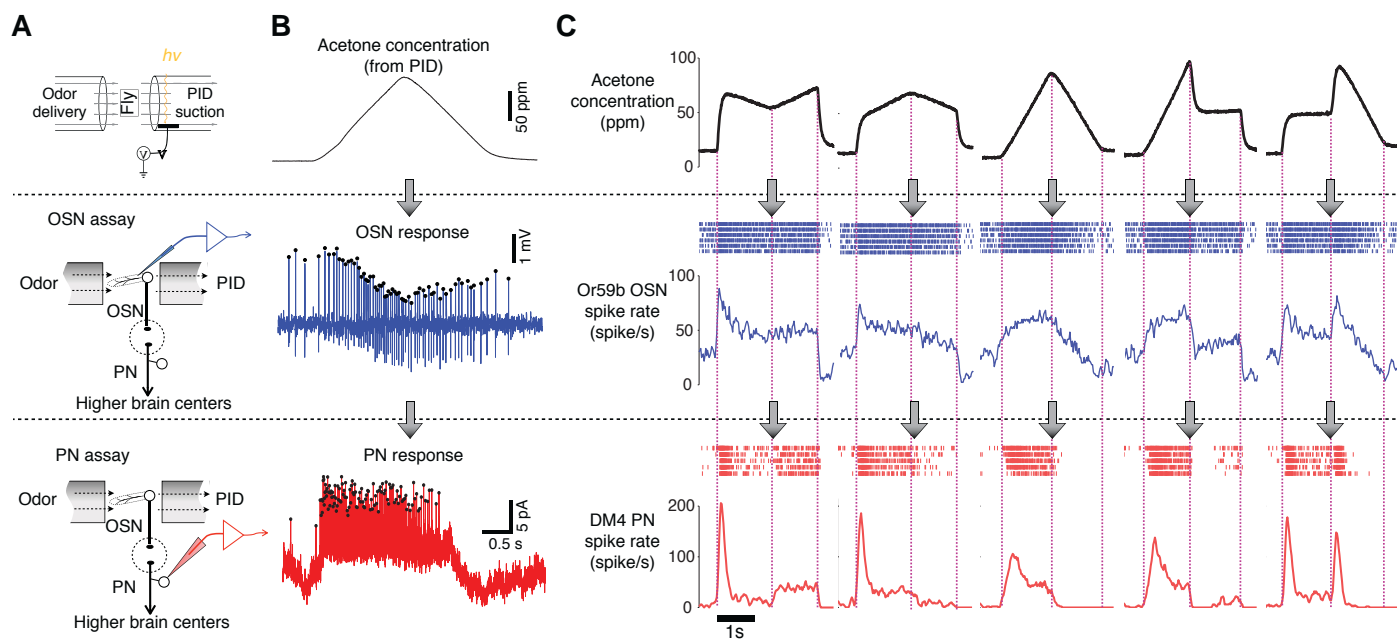


Figure 1





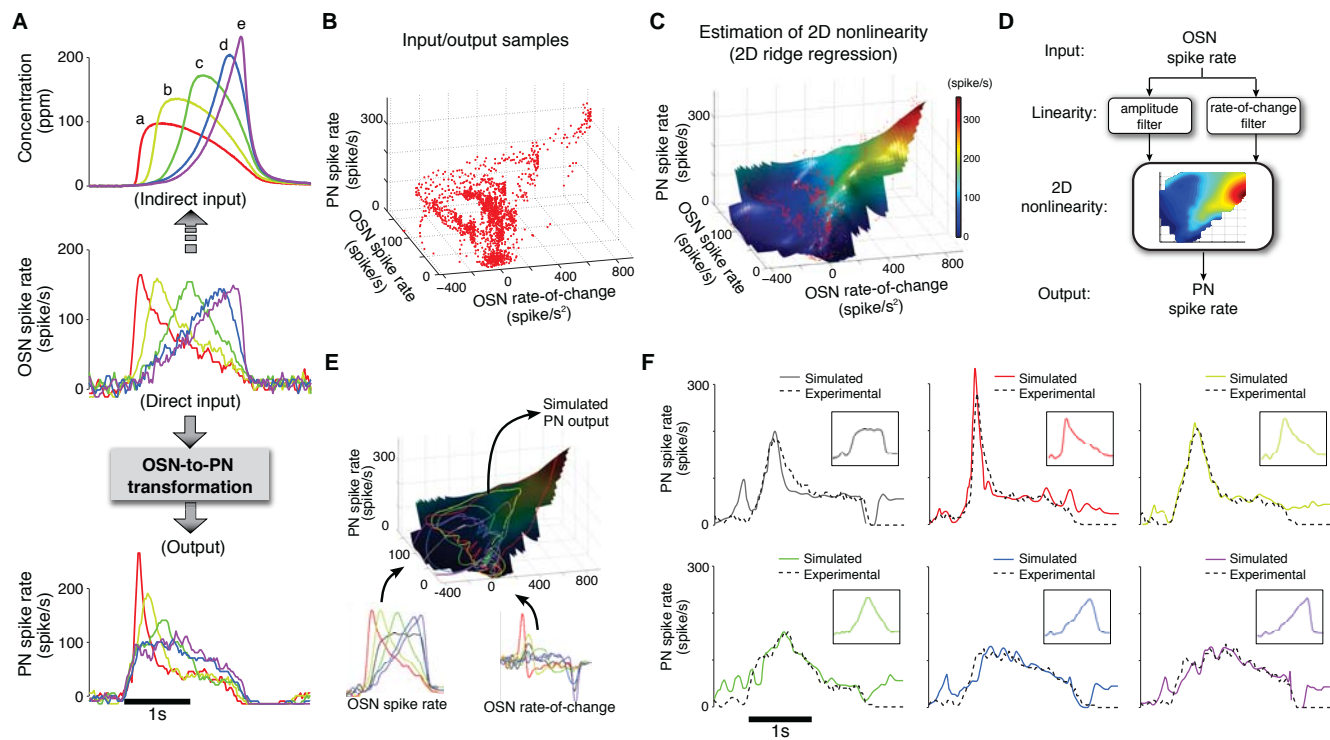


Figure 3

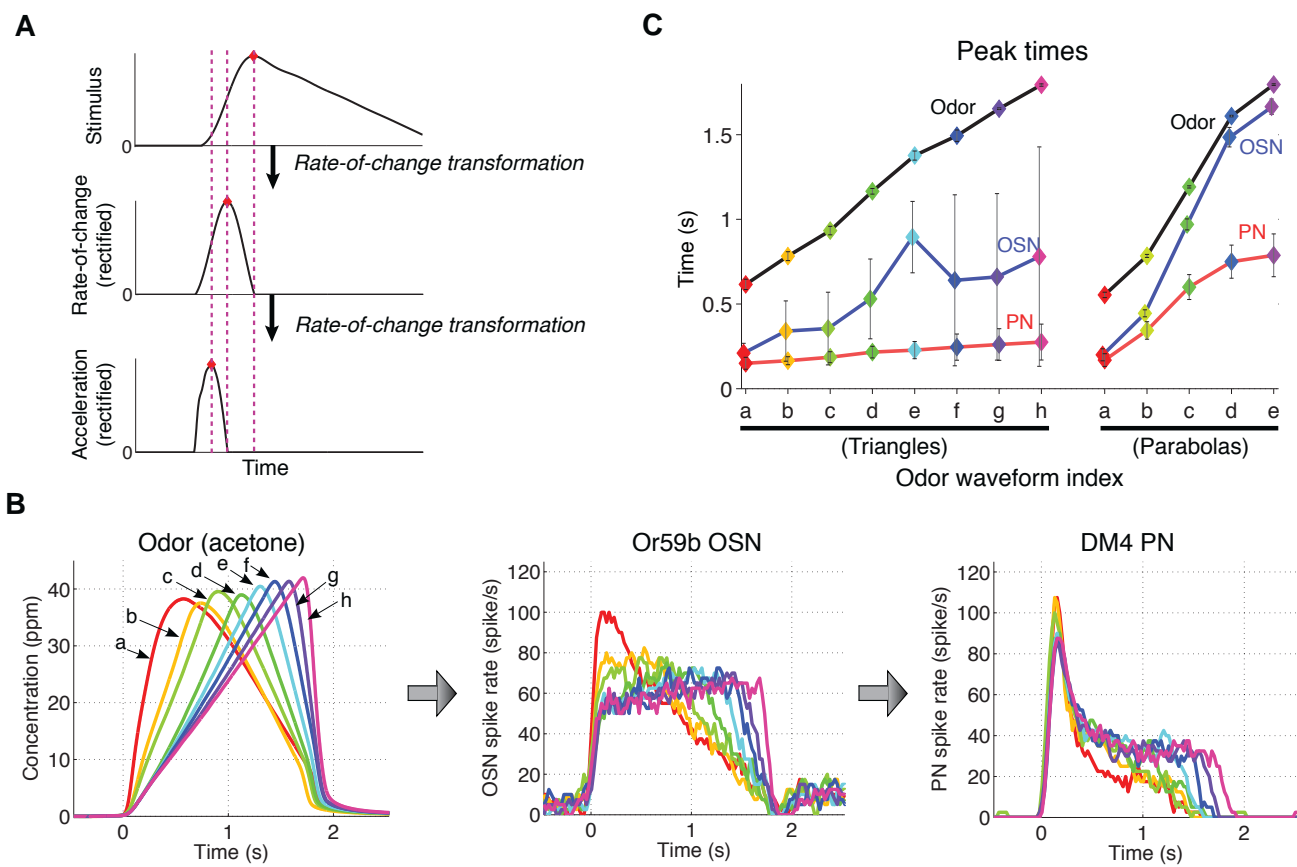


Figure 4